IET Microwaves, Antennas & Propagation

Research Article

IET Journals
The Institution of Engineering and Technology

Dual-segment S-shaped aperture-coupled cylindrical dielectric resonator antenna for X-band applications

ISSN 1751-8725
Received on 28th January 2015
Revised on 23rd June 2015
Accepted on 13th July 2015
doi: 10.1049/iet-map.2015.0076
www.ietdl.org

Asmaa H. Majeed[1], Abdulkareem S. Abdullah[1], Fauzi Elmegri[2], Khalil Hassan Sayidmarie[3], Raed A. Abd-Alhameed[2] ✉, James M. Noras[2]

[1]*Department of Electrical Engineering, College of Engineering, University of Basrah, Basrah, Iraq*
[2]*School of Electrical Engineering and Computing Sciences, University of Bradford, Bradford BD7 1DP, UK*
[3]*Department of Communication Engineering, College of Electronic Engineering, University of Nineveh, Mosul, Iraq*
✉ *E-mail: r.a.a.abd@bradford.ac.uk*

Abstract: A new low-cost dual-segmented dielectric resonator (DR) antenna design is proposed for wideband applications in the X-band region. Two DRs coupled to an S-shaped slot introduce interesting features. The antenna performance was characterised in terms of the reflection coefficient, gain, and radiation pattern, and detailed simulation studies indicate excellent antenna performance from 7.66 to 11.2 GHz (37.5% fractional bandwidth) with a maximum gain of 6 dBi at 10.6 GHz, whereas the fabricated prototype has a matched bandwidth from 7.8 to 11.85 GHz (41% fractional bandwidth) and maximum gain of 6 dB_i. The antenna is compact, size $1 \times 0.83 \times 0.327$ times the wavelength at 10 GHz. The two DR segments may be located on the same side or on opposite sides of the substrate, giving, respectively, improved gain or more uniform field patterns. Experimental testing of the prototype performance showed reasonable agreement with the predicted performance.

1 Introduction

Dielectric resonator antennas (DRAs) have been extensively studied due to their beneficial characteristics: high radiation efficiency, low weight, and small size resulting from the high permittivity of the DR material. One fundamental difference between a DRA and a conventional radiator is that the main loss in the DRA is dielectric loss, and with modern ceramic materials this loss can be made very low [1, 2]. The loss can also remain very small for high permittivity ceramics, so there is no same penalty for miniaturisation that one would expect with metal or metallised radiators. Nevertheless, DRAs are still believed to be subject to the fundamental size/shape/bandwidth trade-off [3–16].

The various techniques that have been utilised to obtain larger bandwidths are monopole geometries [4], DRs with multiple segments of different permittivities [5, 6], and DRs using composite shapes such as the letters H, P or asymmetrical T [7–9], and a cylinder with a bowtie-shaped base [10]. While such shapes are tailored in the design stage to give higher bandwidths, designs using DRs of conventional shapes are still competitive. A microstrip-fed stepped patch with an intermediate substrate has also been used to increase the bandwidth [11]. The use of dual-segment DRs of different permittivities fed by the same line has shown improved bandwidth [12, 15]. Moreover, it has been shown recently that dual similar DRs placed asymmetrically with respect to the feeding aperture can give an increase in the bandwidth as well as offering more design flexibility [3, 16].

In this paper, a new dual-segmented DRA with internal S-shaped slot coupling is proposed for use in X-band communications. Most published papers have used short slots (of length comparable with the diameter of the DR) while this design introduces a much longer slot. The folding of the slot into an S shape offers long electrical length at compact size and utilises its capability of resonating at multiples of the fundamental frequency. The slots used formerly are non-resonating since they are short (less than half the guide wavelength). The bandwidth of the proposed design is thus enhanced by introducing multi-resonant elements such as the S-shaped slot and its coupling structure in addition to the two separated DRs. The design procedure uses several design rules, with analysis and optimisation being carried out using computer simulation technology (CST) Microwave Studio [17]. The realisation also exploits some well-known techniques developed for physically small, low profile, mobile handset, and terminal antenna designs.

2 Antenna layout and construction

The general layout of the DRA assembly is given in Fig. 1, with two identical DRs mounted on a 30 mm × 25 mm substrate-backed ground plane. The resonators are 6 mm (D) × 9 mm (h) cylindrical posts from Dynamic-Ceramic Ltd., Dynallox aluminium oxide (99.7% purity, with $\varepsilon_{dr} = 9.4$ and $\tan\delta = 0.00045$), and the dielectric substrate is an FR4 ($\varepsilon_{subs} = 4.5$, $\tan\delta = 0.002$) of thickness $t = 0.8$ mm. The antenna thus has a compact size of $1 \times 0.83 \times 0.327$ of the wavelength at 10 GHz frequency. The two DRs are excited by the electric field lines at the outer segments of the S-shaped slot. The excitation is in the dual hybrid electric and magnetic $(HEM)_{11\delta}$ mode, for which the structure parameters and resonance frequency are related through the curve-fitted equation

$$f(\text{GHz}) = \frac{30}{2\pi a \varepsilon_{dr}^{0.42}}(1.6 + 0.513z + 1.392z^2 - 0.575z^3 + 0.088z^4) \quad (1)$$

where $a = D/2$ (centimetres) and $z = a/2$ h [1, 13]. This equation can give accurate predictions of the resonance frequency for a wide range of materials and $0.1 < z < 2.5$ [1].

The antenna assembly is excited using an L-shaped microstrip line that is coupled to an S-shaped slot. The feed line dimensions are $L_f = 19.5$ mm, $L_{fl} = 4.2$ mm, and $W_f = 1.5$ mm, as calculated using the standard formulae [18]. The internal coupling mechanism into the two DR resonators is provided through the S-shaped slot. This configuration serves to influence the resonant structure, and the amount of undesired radiation in the backward direction. It also acts to control the coupling between the radiator and the feed.

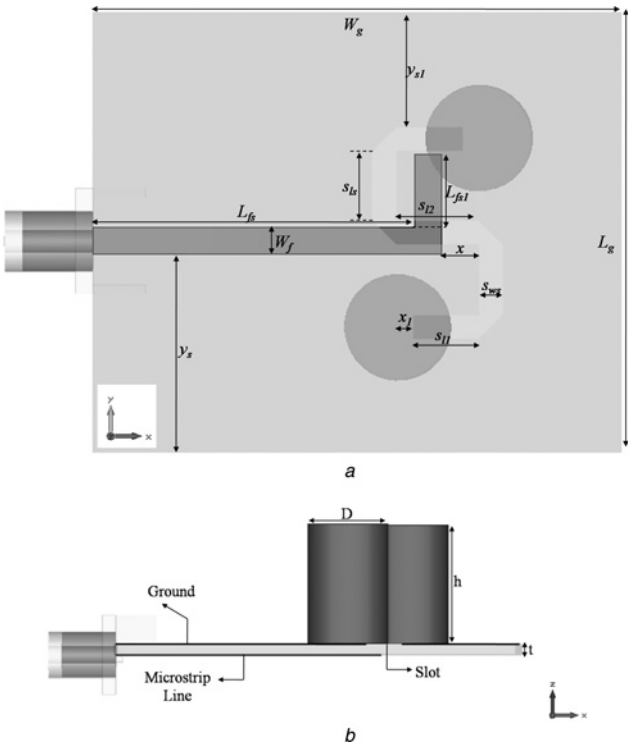

Fig. 1 *Schematic diagram for the dual-segment S-shaped aperture-coupled cylindrical DRA*

a Top view, with structural parameters
b Side view, with structural parameters

3 S-shaped slot

Most published papers have used short slots of lengths comparable with the diameter of the DR, where rectangular, elliptical, and I-shaped slots were employed. These short slots are non-resonating. The slot used here is much longer, and thus resonance can occur at more than one frequency across the band of operation. As shown in Fig. 1 the slot length S_L can be given by

$$S_L = 2 \times S_{l1} + 2 \times S_{ls} + S_{l2} + 4 \times L_b \tag{2}$$

where L_b is the length of each of the four bevelled 90° bends. At resonance, the slot length S_L is equal to N multiples of half the guided wavelength λ_g, that is

$$S_L = N\lambda_g/2 = \frac{N\lambda_o}{2\sqrt{\varepsilon_e}} \tag{3}$$

$$\varepsilon_e \simeq \frac{\varepsilon_{subs} + 1}{2} \tag{4}$$

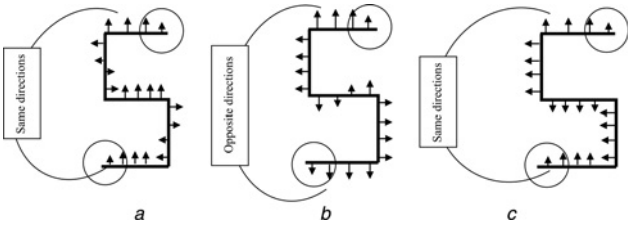

Fig. 2 *Schematic illustration of the electric field distributions along the S-shaped slot for various operating frequencies*

a $S_L = 1.5\lambda_g$
b $S_L = \lambda_g$
c $S_L = 0.5\lambda_g$

where ε_{subs} and ε_e are the permittivities of the substrate and the effective permittivity in the slot, respectively, and λ_o is the free-space wavelength. Thus, the resonance frequency f is given by

$$f = \frac{N_c}{S_L\sqrt{2(\varepsilon_{subs} + 1)}} \tag{5}$$

where c is the speed of light. Equation (5) can be used either to estimate the resonance frequency of a slot or to find the proper slot length at a given resonance frequency. The accuracy of this equation depends on the accuracy of estimating the effective permittivity given by (4), as well as on properly accounting for the four bevelled 90° bends of the S-shaped slot. The placement of the two DRs on the outer segments of the S-shaped slot pulls more E-field lines from the slot toward the DR, since the DR has larger permittivity compared with that of the substrate. Therefore, the effective permittivity in the whole slot will be slightly higher, which leads to a slightly lower resonance frequency than that predicted by (5), which was derived assuming that there were no DRs.

Another interesting feature of the S-slot can be seen by looking at the electric field lines across the slot, as shown in Fig. 2. Three cases – one at the fundamental resonance frequency f_1 and then two at the next modes f_2 and f_3 (i.e. at slot lengths of 0.5, 1, and 1.5 of the guide wavelengths) are shown. It can be seen from this figure that the E-field lines at the outer segments of the slot (under the two DRs) are in the same direction at the fundamental frequency f_1, and its third harmonic $3f_1$ (i.e. when $S_L = \lambda_g/2$ and $1.5\lambda_g$) and hence the two DRs are excited in phase. However, when $N = 2$ (i.e. $S_L = \lambda_g$) the E-field lines will be in opposite directions, and the two DRs are excited in out-of-phase fashion. For the dimensions shown in Table 1 and the FR4 substrate used, it can be shown (from (5)) that the fundamental resonance frequency of the slot is $f_1 = 3.768$ GHz, and the next frequencies are 7.536 and 11.304 GHz.

4 Simulation and parametric analysis

A detailed model of the antenna performance is constructed using CST Microwave Studio. Systematic parameter sweeps are made on each of the principal structure parameters governing the S-shaped slot coupling in turn, whereas the others are held constant; see Table 1. The antenna performance is initially characterised in terms of the reflection coefficient as illustrated in Figs. 3*a–d*. The effects of the various design parameters on the reflection coefficient response are discussed as the follows.

Fig. 3*a* shows the variation in the reflection coefficient (S_{11}) with frequency for various vertical slot lengths, s_{ls}, with $s_{l1} = 3.5$ mm, $s_{ws} = 1.1$ mm, and $x = 1.5$ mm. As the vertical slot length increases, the three resonance frequencies decrease, while the bandwidth and matching change. The optimal value for the vertical slot length appears to be 3.75 mm, as can be seen from the wider impedance bandwidth and minimum reflection coefficient across the frequency range. Fig. 3*b* shows the variation of the reflection coefficient with frequency for different values of the horizontal slot length, s_{l1}, with $s_{ls} = 3.75$ mm, $s_{ws} = 1.1$ mm, and $x = 1.5$ mm. It can be seen that the three resonant frequencies change in different ways and impedance bandwidth decreases with reducing values of s_{l1}, and the optimal value for s_{l1} is 4 mm. Fig. 3*c* shows the variation of the reflection coefficient with slot width, s_{ws}, with $s_{ls} = 3.75$ mm, $s_{l1} = 4.0$ mm, and $x = 1.5$ mm. The primary effect is on the reflection coefficient, and a slight change in the impedance bandwidth can be observed on the upper band-edge. The optimal slot width appears to be 1.2 mm. Fig. 3*d* monitors the effect of the

Table 1 Detailed dimensions (in millimetres) for the proposed antenna

W_g	L_g	D	h	L_f	L_{f1}	y	W_f	s_{l2}	y_1	x_1
25	30	6	9	19.5	4.2	11.25	1.5	4.5	6.5	0.9

IET Microw. Antennas Propag., 2015, Vol. 9, Iss. 15, pp. 1673–1682

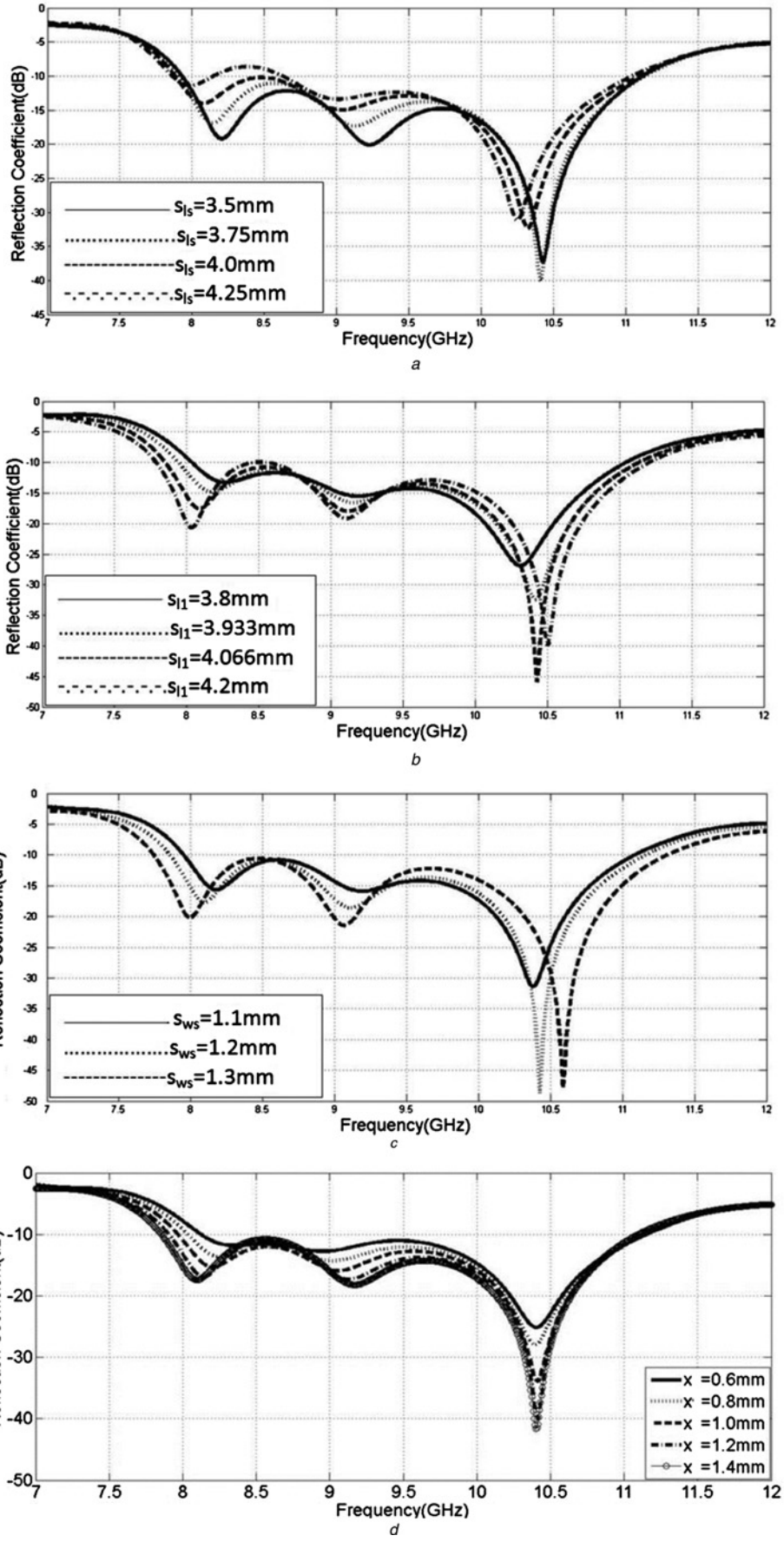

Fig. 3 *Simulated reflection coefficients vs. frequency for different*

a Vertical slot lengths s_{ls}
b Horizontal slot lengths of the two slot ends s_{l1}
c Slot widths s_{ws}
d Position of *S*-slot along feeding line *x*

Table 2 Optimum dimensions (in millimetres) for the prototype antenna assembly

W_g	L_g	D	h	L_f	W_f	L_{f1}	x_1	y	s_{ls}	s_{l1}	s_{l2}	x	y_1	s_w
30	25	6	9	19.5	1.5	4.2	0.9	11.25	3.75	4	4.5	1.2	6.5	1.2

relative positioning of the *S*-slot with respect to the feed line on the reflection coefficient; this is the x parameter in Fig. 1 (in this case $s_{ls} = 3.75$ mm, $s_{l1} = 4.0$ mm, and $s_{ws} = 1.2$ mm). The lower resonance frequency is more affected by the variation, whereas at the other two resonance frequencies the effect is mainly on matching. The optimum position is given by $x = 1.2$ mm.

Fig. 3 shows that there are three resonance frequencies around 8, 9, and 10.5 GHz. The first feature of the reflection coefficient results shown in Fig. 3 is the large dip at about 10.5 GHz, which indicates best matching. The good matching at this frequency is due to two factors. First, for the DR used, (1) estimates a resonance frequency of 10.695 GHz. Referring to Section 3, it can be seen that the slot resonates in the third harmonic at 11.304 GHz as estimated by (5). Thus, the combined effects of the above two factors have resulted in the deep dip at about 10.5 GHz. The second feature of the reflection coefficient results shown in Fig. 3 is the large value of S_{11} (high mismatch) for the 7.0–7.5 GHz range of frequencies. The analysis of Section 3 predicts that there is out-of-phase excitation for the two DRs at a frequency of 7.536 GHz where the slot resonates at the λ_g mode.

5 Prototype measurements

A prototype DRA assembly was constructed using the parameter values derived from the previous section, and these are listed in Table 2. Front and back views of the prototype are shown in Fig. 4. The reflection coefficient was measured using a vector network analyser (HP8510C) and results for antenna assemblies with and without DR posts present are summarised in Fig. 5, alongside the corresponding simulation data. When there are no resonant posts on the slot side, the measured impedance bandwidth, for $S_{11} \leq -10$ dB, is extended from 11.2 to 12.6 GHz, that is, the fractional impedance bandwidth is 11%. This frequency range confirms the third mode resonance of the slot of 11.304 GHz. Introduction of two DR posts on the slot side produces a bandwidth from 7.8 to 11.85 GHz, a fractional bandwidth of 41%. In the simulation, the corresponding values were found to be 9 and 37.5%. The addition of the DR posts improves the reflection coefficient and impedance bandwidth. The simulated and measured data show multiple resonances, which can account for this extended wide bandwidth performance. Results measured without the two DRs show good agreement with the simulation results. However, the deep null occurs at 11.91 and 11.062 GHz for the measured and CST results, respectively. This resonance frequency corresponds to a slot resonance at $1.5\lambda_g$ (11.304 GHz) as predicted by (5) and the prediction errors were found to be 5.4 and −2.1%, respectively. With the two DRs the right dip occurs at 10.5 and 10.7 GHz for the simulation and measured results, respectively, which are lower than the value predicted by (1) by only 1.8 and 0.5%, respectively.

The results of Fig. 5 show that at 9 GHz the reflection coefficient value is −20 dB (very good matching) for the CST results, whereas it is −10 dB in the measurement results. The measurement process usually adds some mismatches that degrade the $|S_{11}|$ value. However, both cases are considered as matched ones assuming −10 dB (voltage standing wave ratio < 2) criterion.

Fig. 6 compares the simulated and measured gains in the broadside direction for the same configurations as above. Good agreements between the measurement and simulation results are noted both with and without the DRs. The maximum simulated gain with no DR present is 5.3 dB_i at 11.2 GHz, and with the two DR posts mounted on the slot side it is 6 dB_i at 10.6 GHz. The corresponding measurements are 5 dB_i at 11.2 GHz and 6 dB_i at 10.6 GHz, respectively. On average, these measurement results are consistent with the values predicted from the parametric modelling. It can also be seen that there is an improvement of ∼4 dB in the gain across the operational band. This improvement in gain is attributed to the use of the two DR posts, which are fed in phase. Comparing the gain values obtained from the CST simulations and measurement with the two DRs, Fig. 6 shows that the gain values differ by <0.9 dB across the frequency range 7.5–11 GHz. At 9 GHz the antenna gain obtained from CST simulation

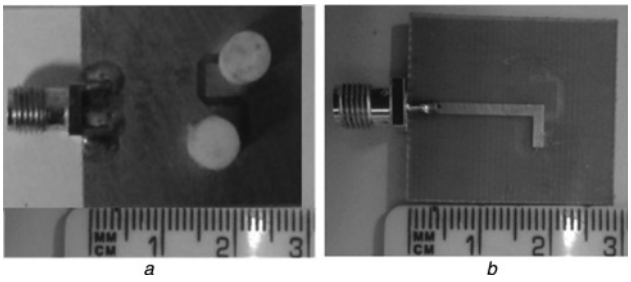

Fig. 4 *Photographs of the prototype antenna*

a Front view
b Back view

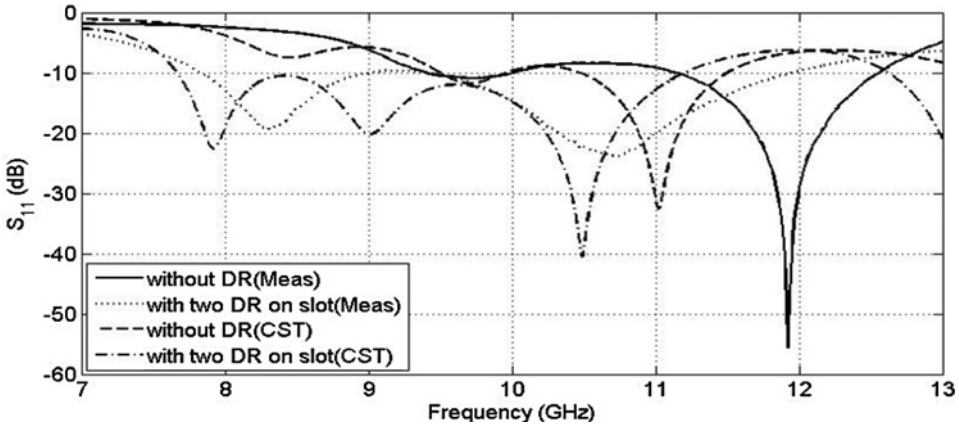

Fig. 5 *Simulated and measured reflection coefficients vs. frequency for the antenna*

IET Microw. Antennas Propag., 2015, Vol. 9, Iss. 15, pp. 1673–1682

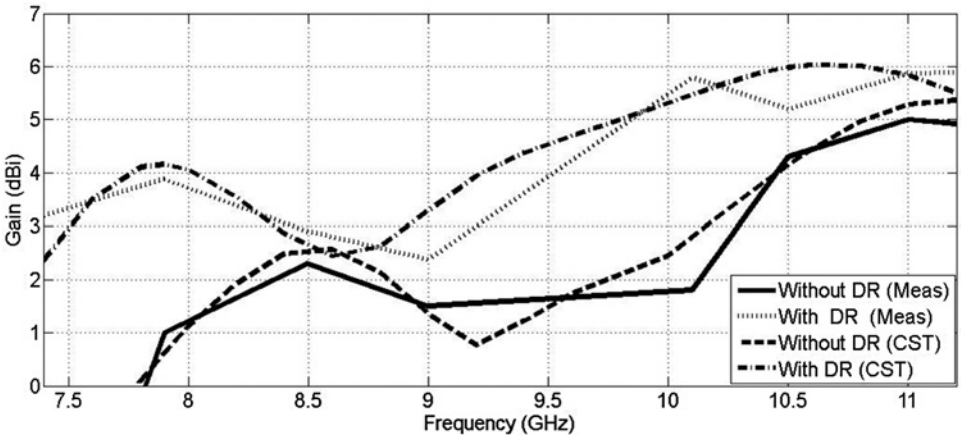

Fig. 6 *Comparison of simulated and measured antenna gains for the proposed antenna*

is about 0.9 dB higher than that obtained from measurements. In general, the measured values of gain are lower than those found from CST simulations.

Desirable design features such as high gain, wide radiation pattern, and large bandwidth cannot be achieved easily at the same time. An application may not require all of these desirable features. While Thamae and Wu [10] and Coulibaly [11] have achieved fractional bandwidths of 50 and 49.4% respectively, and gains of 4–7 dB, in [11] the two antennas have large sizes, compared with the proposed antenna, due to their large ground planes: a large ground plane increases the front/back ratio of the radiation pattern and enhances the gain. Although higher gains of 5–7 dB_i were achieved in [19, 20] using only single DRA geometries, the proposed antenna with two DRs has 41% bandwidth compared with 3.6% in [19] and 26.8% in [20]. Moreover, the proposed antenna offers much more uniform radiation patterns and smaller size. Further comparison with the published works is presented in Table 3. While some complex shapes are tailored in the design stage to give the desired high bandwidths, designs using readily available DRs of conventional shapes are still competitive. It can be seen that the proposed antenna does have competing gain and bandwidth, whereas at the same time it has the second smallest size among the listed antennas, namely $(1 \times 0.83 \times 0.327)$ times the wavelength at 10 GHz.

The other feature that can be concluded from Fig. 6 is that the antenna gain drops drastically for frequencies below 7.5 GHz for the case without DRs, and below 7 GHz with DRs. This drop is caused by the fact that at a frequency of $2f_1 = 7.536$ GHz, the *E*-field lines under the two DRs are in opposite directions (see Fig. 2*b*) leading to out-of-phase excitation of the DRs. The net effect is a null or reduced radiation in the broadside direction. Even without the two DRs, the segments of the slot have *E*-field lines that are in opposite directions, causing a reduction in the power radiated from the slot and hence small gain.

The far-field radiation patterns of the prototype antenna were measured in an anechoic chamber using an elevation-over-azimuth positioner, with the elevation axis coincident with the polar axis $\theta = 0°$ of the antenna-under-test (AUT) coordinate system. The reference antenna was a broadband horn (EMCO type 3115) positioned 3.5 m from the AUT. Two pattern cuts (i.e. the *xz* and *yz* planes) were taken at three selected operating frequencies (7.92, 9, and 10.49 GHz), covering the complete designated bandwidth. The simulated and measured radiation patterns are compared in Fig. 7. The patterns show fairly uniform variation in the *xz* and *yz* planes, with some ripples that increase at higher frequencies. The patterns look slightly unsymmetrical due to the asymmetry in the layout of the slot and feed lines. The cross-polar patterns are low in the *xz*-plane at lower frequency but relatively high at upper frequencies. The relatively high level of the cross-polar radiation may be caused by the slot being twisted into an S-shape. Although there are two radiating DRs in the *yz*-plane, the array feature does not appear as the two elements are separated by 0.35 wavelengths at 10.49 GHz frequency. The computed radiation patterns are in reasonable agreement and are consistent with the measurements.

6 Magnitudes of electric and magnetic fields

The magnitude variations in the electric and magnetic fields were calculated in the simulation for the optimised antenna model at frequencies of 10.5 and 11.34 GHz. The *E*-field and *H*-field distributions were calculated across a plane that is parallel to the *z*-axis and passing through the axis of one of the two cylindrical DRs: see Fig. 8*a*. The field distributions for the other DR are similar and thus for brevity are not shown here. At a frequency of 10.5 GHz, the *E*-field and *H*-field lines are orthogonal, and both are parallel to the cylindrical DR base. These features are consistent with those of the $HEM_{11\delta}$ mode [1, 13], whose frequency was predicted by (1). Away from resonance frequency (i.e. at 11.34 GHz) the *E*-field lines are perpendicular to the DR base, whereas the magnetic field lines are parallel to the base of the DR.

It should be noted here that the obtained distributions are not very similar to those depicted in text books. This can be attributed to the fact that the field distributions for an isolated DR will not be the same as those when the DR is placed on a coupling aperture due to the

Table 3 Comparison of the proposed antenna characteristics with those of published works

References	DR type	Centre frequency, GHz	Percentage bandwidth	Gain, dB_i	Antenna size, mm^3
[7]	H-shaped DR, $\varepsilon_r = 9.8$	5.23	62	N.A.	$55 \times 60 \times 13.5$
[8]	P-shaped DR, $\varepsilon_r = 10.2$	5.85	80	3.4–4.2	$17 \times 35 \times 6.7$
[9]	asymmetrical T-shaped DR, $\varepsilon_r = 9.8$	6.1	75.1	3.24–7.35	$60 \times 60 \times 13.6$
[10]	rectangle $\varepsilon_r = 10.2$	10.16	50	NA	$40 \times 52 \times 4.61$
[11]	cylinder with bowtie base $\varepsilon_r = 9.8$	5.569	49.4	4–7	$60 \times 60 \times 13.5$
[12]	rectangle, two segments	5.39	76.8	0–1	$50 \times 50 \times 13$
[19]	circular disk $\varepsilon_r = 82$	4.18	3.6	5	$140 \times 150 \times 2.8$
[20]	cylinder $\varepsilon_r = 12$	10	23.7	6–7	$80 \times 80 \times 9.8$
this work	two cylinders, $\varepsilon_r = 9.4$	9.6	41	4–6	$25 \times 30 \times 9.8$

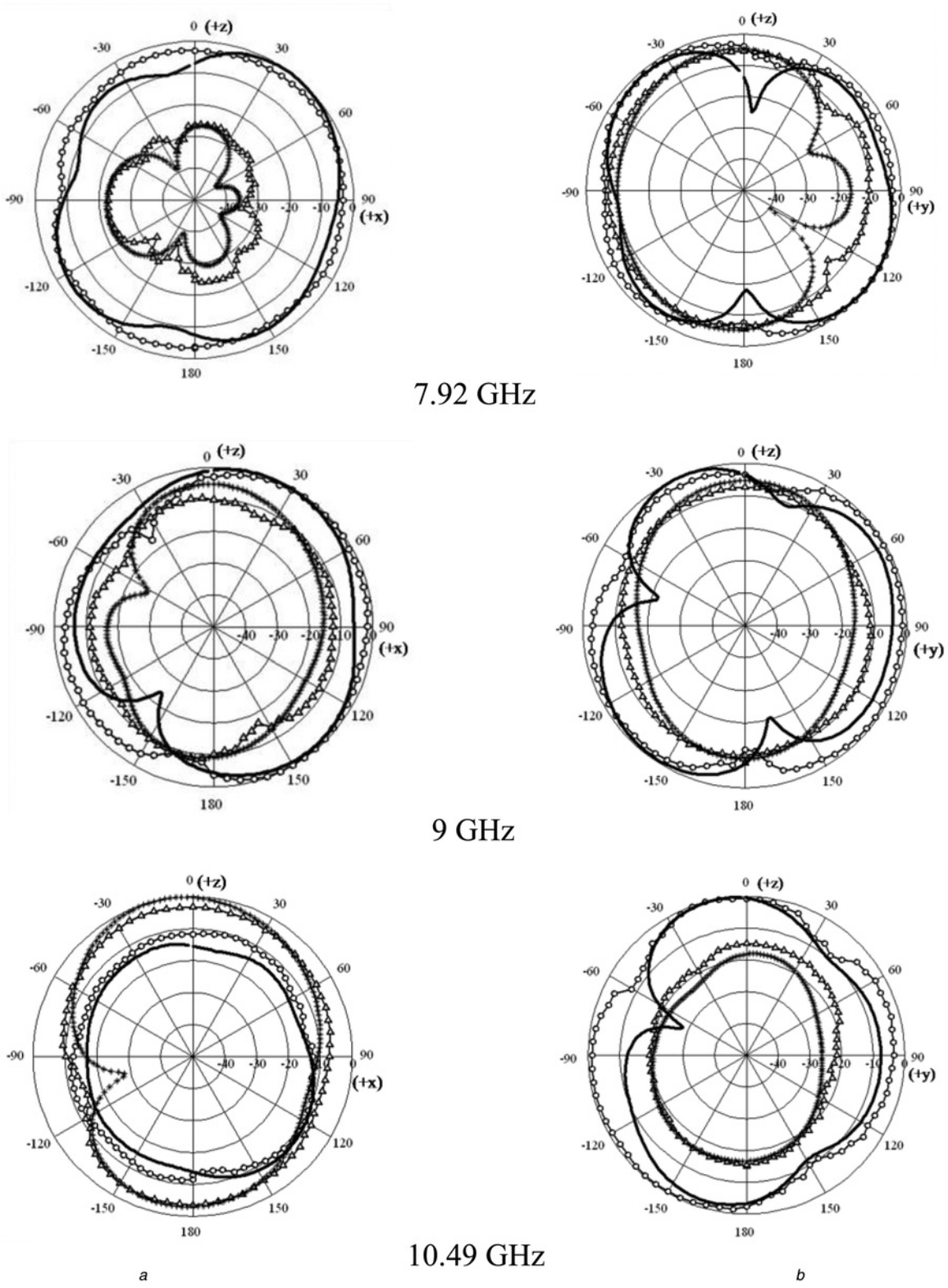

Fig. 7 *Far-field radiation patterns at*

a xz-plane
b yz-plane
E_θ meas. (solid-circles), E_ϕ Meas. (triangle), E_θ CST (solid), and E_ϕ CST (solid-*)

proximity effect of the feeding aperture. Another factor is that the second DR is only 0.37 of a wavelength (at 10 GHz) away from the first one where field lines are coupled to each other.

Further assessment of the above field distributions, see Fig. 8*b*, shows that the maximum of the *E*-field is 3.95×10^4 V/m at the 10.5 GHz resonance frequency of the DR, whereas it is 2.86×10^4 V/m at 11.34 GHz, the slot resonance. The maximum of the *E*-field at the DR resonance is 1.38 times that is found at the slot resonance frequency. The 1.38 magnitude ratio corresponds to a frequency ratio of only 1.08.

The corresponding ratio for the magnetic field intensities is 1.27. Such high peaking in *E*-field and *H*-field responses is usually

IET Microw. Antennas Propag., 2015, Vol. 9, Iss. 15, pp. 1673–1682

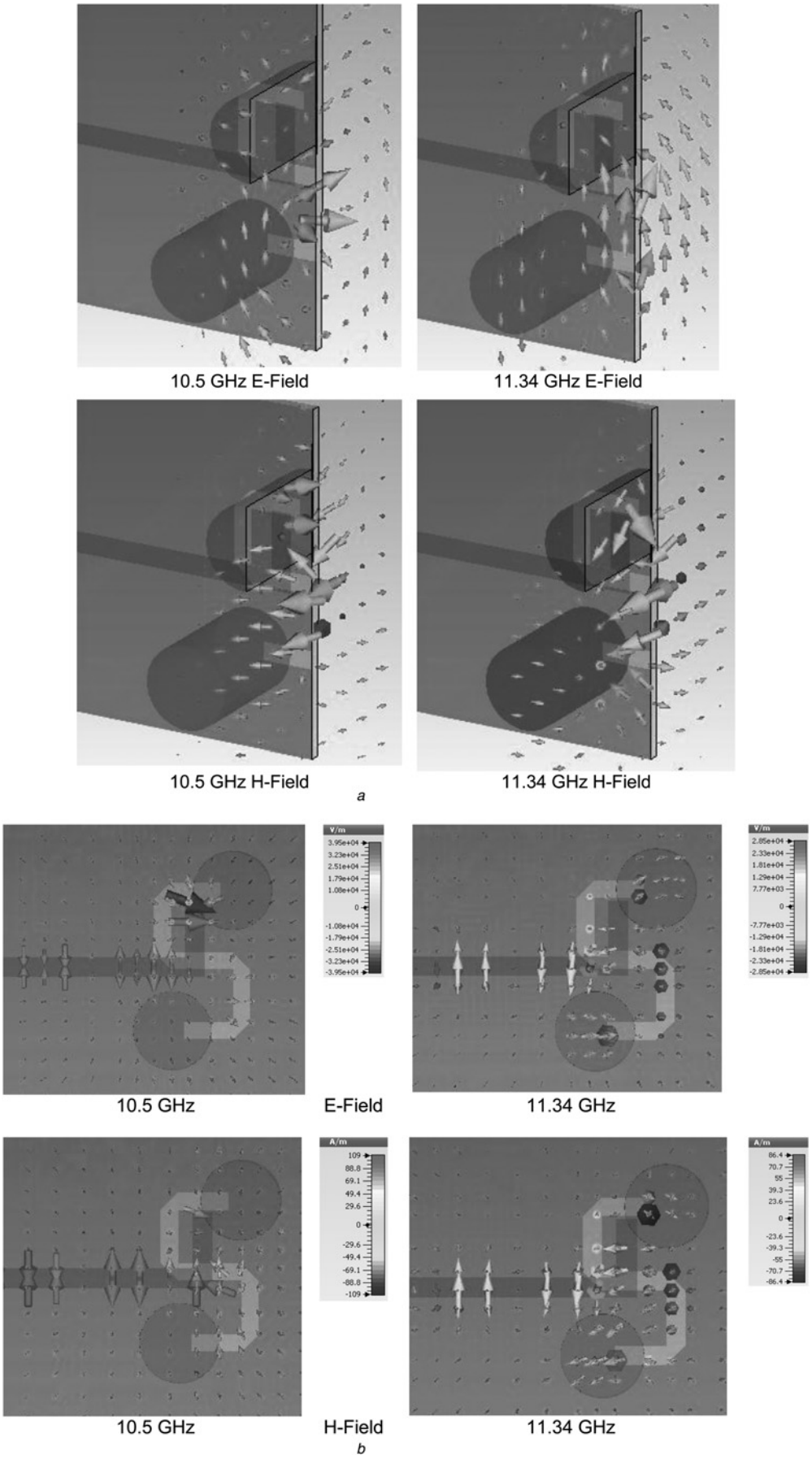

Fig. 8 *Distributions of the electric and magnetic fields of the dual-segment antenna*

a Across the plane that is parallel to the *Z*-axis and passing through axis of one of the two cylindrical DRs
b Magnitude variations across the *xy*-plane passing at 1 mm below the upper base of the DRs (at $z = 8$ mm)

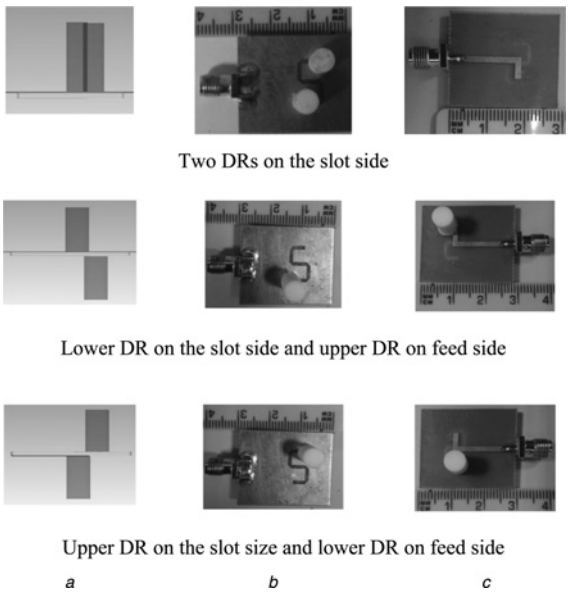

Fig. 9 *Investigated positions of two DRs*

a Simulated model
b Fabricated antenna showing slot side
c Fabricated antenna showing feed side

attributed to a resonance process. These findings are in line with the prediction of the base mode frequency from (1), namely, 10.695 GHz, where the dominant mode at this frequency is HEM_{110}.

7 Positioning of the DRs

The proposed feed arrangement with the S-shaped slot enables various placements of the two DRs, whose relative positioning needs to be considered in more detail. A refinement of the parametric study in Section 4 was made by considering the three configurations shown in Fig. 9: (i) both resonators on the slot side, (ii) upper resonator on the slot side and lower resonator on the feed side, and (iii) upper resonator on the feed side and lower resonator on the slot side. It is worth noting that positioning of the DR on the conductor side of the slot is different from when the DR is put on the substrate side of the slot. The latter case introduces a thin layer (0.8 mm of $\varepsilon_{subs} = 4.5$) under the DR, which can be considered as a two-layered DR leading to a slightly different resonance frequency. Therefore, placement of the two DRs on opposite sides can result in slightly different resonance frequencies and a different antenna radiation pattern in comparison with the case when both DRs are on the same side. The performances of the three configurations are shown in Fig. 10 for the simulated model and the prototype DRA. In Fig. 10, it can be seen that case (i) delivers 41 and 37.5% measured and simulated

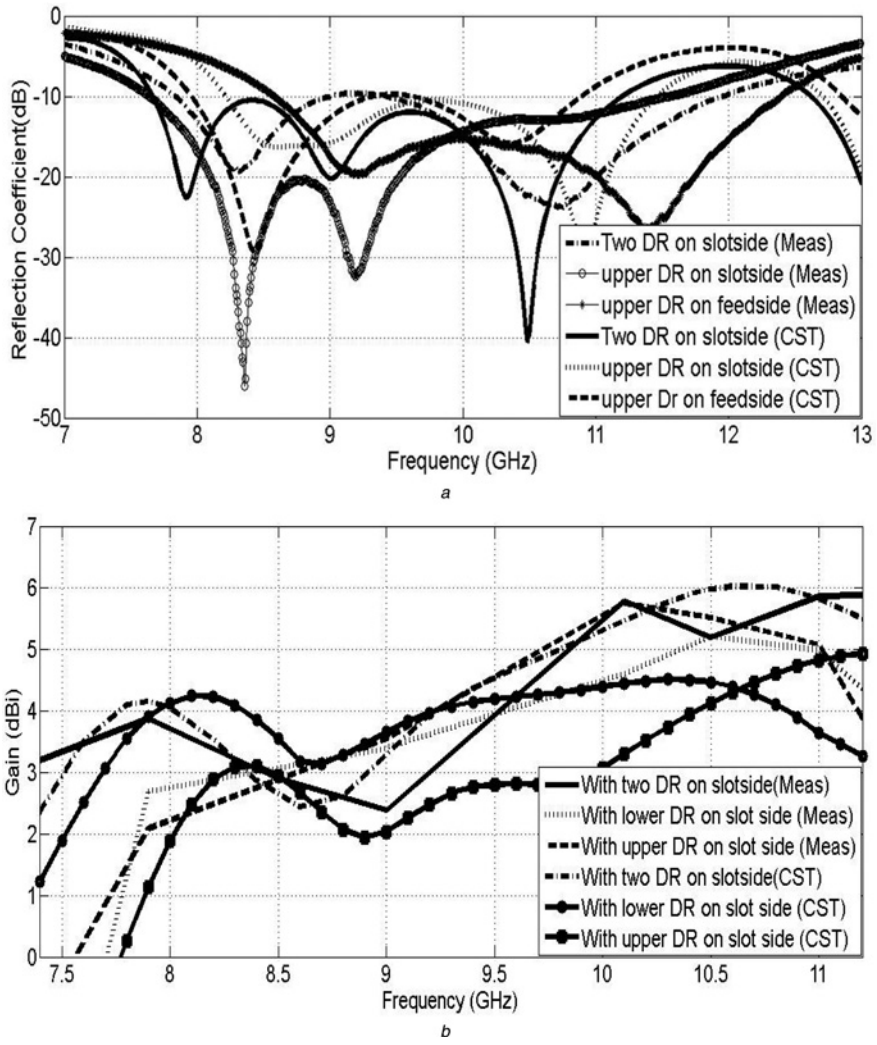

Fig. 10 *Simulated and measured*

a Reflection coefficient magnitude (S_{11})
b Gain (dB_i) vs. frequency plots with different DR positions

IET Microw. Antennas Propag., 2015, Vol. 9, Iss. 15, pp. 1673–1682

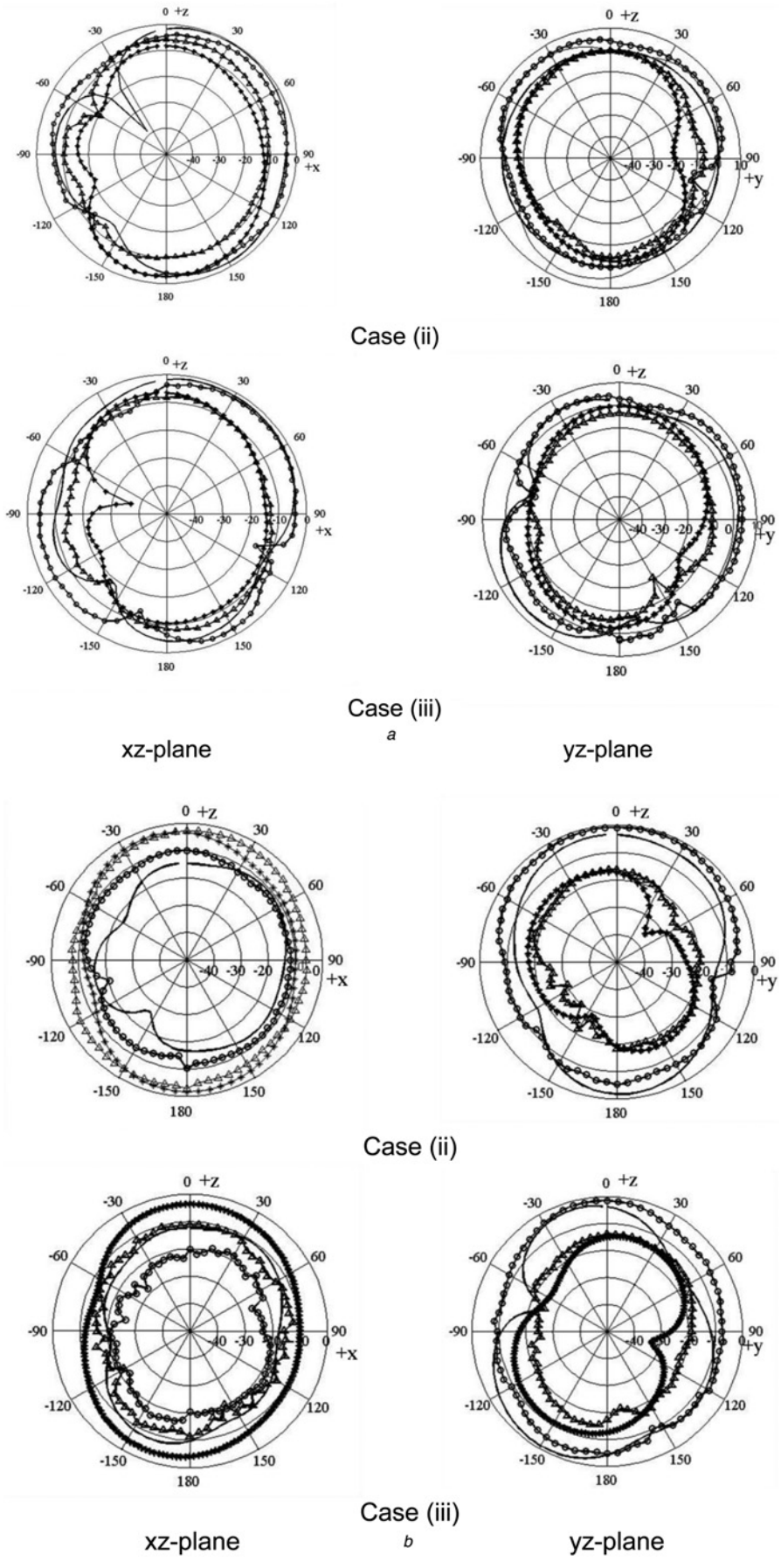

Fig. 11 *Measured and simulated far-field radiation patterns for two antenna arrangements (ii) and (iii) shown in Fig. 9, at*

a 9 GHz

b 10.5 GHz

E_θ Meas. (solid-circles), E_ϕ Meas. (triangle), E_θ CST (solid), and E_ϕ CST (solid-*)

bandwidths, respectively. The corresponding maximum gain values are 6 dB_i at 10.6 and 11.2 GHz, respectively. The simulation results show that case (ii) gives 31.7% bandwidth and 4.51 dB_i maximum gain at 10.3 GHz and case (iii) gives 33% bandwidth and 4.92 dB_i maximum gain at 11.2 GHz. Thus, the largest impedance bandwidth and gain are achieved for case (i), where the two DRs are placed on the same side of the substrate. However, case (ii) and case (iii) indicate a better response for the difference between the maximum and minimum gain states that means more uniform patterns but with gain reduced by 1–1.5 dB_i. It should be noted that when placing the two DRs on opposite sides of the substrates (cases ii and iii) no attempt was made for further optimisation of the antenna parameters to achieve better performance. It is also noted that the dips in the reflection coefficient responses differ slightly for the three cases due to the fact that the resonance frequencies are influenced by the relative placement of the slot and DR.

The simulated far-field radiation patterns, for the two cases (ii) and (iii) are presented in Fig. 11, for two operating frequencies, 9 GHz, and 10.5 GHz. Measurements of the radiation patterns were also performed for these two antenna arrangements and plotted on Fig. 11 for comparison. This figure shows fair agreement between measured and simulation patterns. The cross-polarised patterns are relatively high, and this may also be attributed to the slot being twisted into the S-shape. The radiation patterns for case (i) are already displayed in Fig. 7, and for brevity they are not repeated. It can also be seen that case (ii) and case (iii) have wider patterns as compared with case (i). This result can be attributed to the displacement of the two DRs on opposite sides of the substrate.

8 Conclusion

A new, physically compact, aperture-coupled dual-segment DRA has been proposed for use in X-band communications. Identical cylindrical DR posts of permittivity 9.4 are mounted on a substrate-backed ground plane. The antenna is excited using an L-shaped feed line, and internal antenna coupling is achieved using an S-shaped slot. The folding of the slot into an S-shape has offered many interesting features. The measured prototype performance shows a maximum gain of 6 dB_i over the frequency range 7.8–11.85 GHz (41% fractional bandwidth), whereas the simulations gave a fractional bandwidth of 37.5% across the 7.66–11.2 GHz frequency range. The fabricated prototype has suitable radiation patterns. The DR posts may be arranged in two distinct configurations: (i) occupying a space on one side of the substrate and (ii) on opposite sides. The first configuration results in higher gain and greater bandwidth, whereas the second one results in more uniform field distribution but at slightly reduced gain. This is an obvious result of placing two DR radiators in same direction as in (i) or in two opposite directions as in (ii). The antenna can suit applications, for example, in mobile and fixed satellite, radio location, and ultra-wideband orthogonal frequency division multiplexing.

9 Acknowledgments

This work was supported in part by the United Kingdom Engineering and Physical Science Research Council (EPSRC) under grant EP/E022936A and the Iraqi Ministry of Higher Education and Scientific Research.

10 References

1 Luk, K.M., Leung, K.W.: 'Dielectric resonator antennas' (Research Studies Press, Hertfordshire, England, 2003)
2 Petosa, A.: 'Dielectric resonator antenna handbook' (Artech House Publishers, Bolton, 2007)
3 Majeed, A.H., Abdullah, A.S., Elmegri, F., *et al.*: 'Aperture-coupled asymmetric dielectric resonators antenna for wideband applications', *IEEE Antennas Wirel. Propag. Lett.*, 2014, **13**, pp. 927–930
4 Haraz, O.M., Sebak, A.-R., Denidni, T.A.: 'A hybrid printed monopole antenna loaded with dielectric resonator for wideband and circular polarization applications', *Int. J. RF Microw. Comput. Aided Eng.*, 2012, **22**, (5), pp. 588–593
5 Kakade, A.B., Kumbhar, M.S.: 'Wideband circularly polarized conformal strip-fed three layer hemispherical dielectric resonator antenna with parasitic patch', *Microw. Opt. Technol. Lett.*, 2014, **56**, (1), pp. 72–77
6 Guha, D., Gupta, B., Kumar, C., *et al.*: 'Segmented hemispherical DRA: new geometry characterized and investigated in multi-element composite forms for wideband antenna applications', *IEEE Trans. Antennas Propag.*, 2012, **60**, (3), pp. 1605–1610
7 Liang, X.-L., Denidni, T.A.: 'H-shaped dielectric resonator antenna for wideband applications', *IEEE Antennas Wirel. Propag. Lett.*, 2008, **7**, pp. 163–166
8 Khalily, M., Rahim, M.K.A., Kishk, A.A., *et al.*: 'Wideband P-shaped dielectric resonator antenna', *Radio Eng. J.*, 2013, **22**, (1), pp. 281–285
9 Yang, G., Zhenghe, F., Li, Z.: 'Compact asymmetrical T-shaped dielectric resonator antenna for broadband applications', *IEEE Trans. Antennas Propag.*, 2012, **60**, (3), pp. 1611–1615
10 Thamae, L.Z., Wu, Z.: 'Broadband bowtie dielectric resonator antenna', *IEEE Trans. Antennas Propag.*, 2010, **58**, pp. 3707–3710
11 Coulibaly, Y., Denidni, T.A., Boutayeb, H.: 'Broadband microstrip-fed dielectric resonator antenna for X-band applications', *IEEE Antennas Wirel. Propag. Lett.*, 2008, **7**, pp. 341–345
12 Rezaei, P., Hakkak, M., Forooaghi, K.: 'Design of wideband dielectric resonator antenna with a two segment structure', *Prog. Electromagn. Res., PIER*, 2006, **66**, pp. 111–124
13 Kajfez, D., Kishk, A.A.: 'Dielectric resonator antenna – possible candidate for adaptive antenna arrays'. Proc. VITEL 2002, Int. Symp. on Telecommunications, Next Generation Networks and Beyond, Portoroz, Slovenia, 13–14 May 2002
14 Saed, M., Yadla, R.: 'Microstrip-fed low profile and compact dielectric resonator antennas', *Prog. Electromagn. Res. PIER*, 2006, **56**, pp. 151–162
15 Rashidian, A., Klymyshyn, D.M.: 'On the two-segmented and high aspect ratio rectangular dielectric resonator antennas for bandwidth enhancement and miniaturization', *IEEE Trans. Antennas Propag.*, 2009, **57**, (9), pp. 2775–2780
16 Majeed, A.H., Abdullah, A.S., Elmegri, F., *et al.*: 'Rectangular slot-fed asymmetric cylindrical dielectric resonators antenna for wideband applications'. Loughborough Antennas and Propagation Conf. LAPC 2014, 8–11 November 2014, pp. 244–248
17 Microwave Studio Users' Manual, Computer Simulation Technology AG, Darmstadt, 2011
18 Pozar, D.M.: 'Microwave engineering' (John Wiley & Sons, New York, 1998, 2nd edn.)
19 Leung, K.W., Chow, K.Y., Luk, K.M., *et al.*: 'Low profile circular disk DR antenna of very high permittivity excited by a microstripline', *Electron. Lett.*, 1997, **33**, pp. 1004–1005
20 Chair, R., Kishk, A.A., Lee, K.F.: 'Wideband simple cylindrical dielectric resonator antennas', *IEEE Microw. Wirel. Compon. Lett.*, 2005, **15**, pp. 241–243